Hyperspectral imaging thermometry assisted by upconversion nanoparticles: experimental artifacts and accuracy

Eduardo D. Martínez[a,b*], Carlos D.S. Brites[c], Ricardo R. Urbano[d], Carlos R. Rettori[d,e], Luís D. Carlos[c]

[a] *Institute of Nanoscience and Nanotechnology (INN), Bariloche Atomic Centre, National Atomic Energy Commission (CNEA), Av. Bustillo 9500, S. C. de Bariloche, Río Negro, Argentina*
[b] *National Scientific and Technical Research Council (CONICET), Argentina*
[c] *Phantom-g, CICECO - Aveiro Institute of Materials, Department of Physics, University of Aveiro, 3810-193, Aveiro, Portugal*
[d] *"Gleb Wataghin" Institute of Physics (IFGW), University of Campinas (UNICAMP), Campinas, Brazil*
[e] *CCNH, Universidade Federal do ABC (UFABC), Santo André, Brazil*

Abstract

Thermometry at the sub-microscale is a highly desired goal for the study of nanostructures and microbiological systems. Rare-earth doped upconversion nanoparticles constitute ideal elements to act as optical probes for the ratiometric measurement of the local temperature. In this work, we combine the ability of upconversion nanoparticles to operate as luminescent thermometers with hyperspectral microscopy to construct thermal images based on the heat dissipation of a percolating network of silver nanowires containing the nanoparticles under controlled electrical current flow. We quantify the electrothermal action by analyzing the hyperspectral data and constructing 2D maps for the emission intensity, the signal-to-noise ratio, and temperature, concluding that no significant thermal gradients were identified. The thermal evolution is clearly sensed by the upconversion nanoparticles, validating the use of this method for studying slow-dynamical thermal processes. We finally present a discussion about the accuracy of the thermal readings and the systematic limitations of the proposed method.

Keywords: luminescence thermometry, hyperspectral imaging; luminescence; upconversion; transparent conductors; silver nanowires

1. Introduction

The development of new thermometric technologies is essential to explore fundamental concepts in nanoscience and study micro and nanoscopic systems in which heat generation and dissipation occur. Conventional thermometry with thermocouples, thermistors, and transistor-based sensors are, at least, impractical for probing thermal effects in systems with dimensions smaller than few millimeters [1–3]. While microfabrication techniques make it possible to integrate such thermometer at a precise position, the measurement of thermal gradients within the microsystem require multiple sensors. This limitation has pushed forward the development of more sensitive techniques with higher thermal and spatial resolution [1,4–6]. Among these methods, luminescence thermometry – using rare-earth-doped upconversion nanoparticles (UCNPs) – has been proposed and successfully applied in the last decade by different groups [7–10]. The physical basis for the thermometric action of UCNPs was thoroughly revised by Suta *et al.* [11]. On the other hand, optical imaging techniques have evolved to provide metadata superimposed to the regular image, for example, by adding spectroscopic information in each pixel. This constitutes the basis of hyperspectral imaging (HSI) technologies which can be adapted to optical microscopy to resolve optical absorption, scattering, or luminescence phenomena in microstructures and nanoparticles [12–17].

In this work, we combine the thermometric properties of UCNPs with HSI optical microscopy to probe the heat dissipation in a model microstructure formed by self-assembled silver nanowires (AgNWs) with UCNPs deposited on the top. AgNWs form percolating networks on different substrates with high electric conductivities and high transparency, which makes them ideal components for flexible and wearable electronics [18,19], transparent electrodes for organic solar cells [20], strain sensors [21], and many other emerging technologies [22,23]. In particular, AgNWs networks and coatings were investigated as transparent electrothermal elements for the controlled heating of surfaces[23–27]. However, the extended use of AgNWs films has been limited by their thermal degradation during continuous current flows [28,29]. More precisely, the contact resistance formed at the junctions between nanowires has been pointed out as the main source of heat generation causing failure of the percolating network [28,30]. In this work, we develop a thermal imaging method that can reliably sense the eventual thermal gradients and “hot-spots” by combining the ability of UCNPs to operate as luminescent thermometers with HSI. We thoroughly characterized the pros and cons of such a method by performing post-processing image analyses and calculating the accuracy, the statistical fluctuations, and the systematic errors of the experimental set-up.

2. Experimental

2.1 Experimental set-up

The experimental strategy proposed in this work for constructing thermal images is based on covering a model nanostructure with nanoparticles that can act as local luminescent thermometers. The covered sample was placed on the stage of an optical microscope (Olympus BX51 microscope) adapted with an optical fiber entrance for exciting the luminescence of the nanoparticles with a proper laser, a dark field (DF) module acting on the condensation lens, a CCD camera (Retiga 4000R, QImaging) for the acquisition of optical images and a visible and near-infrared (VNIR) spectrophotometer with integrated camera for the acquisition of the emission spectra at each point of the field of view. The CytoViva hyperspectral line-scanning imaging system is constituted by a digital camera (IPX-2M30, Imperx) coupled to a spectrograph (V10E 2/3", Specim, 30 μm slit, nominal spectral range of 400–1000 nm, and nominal spectral resolution of 2.73 nm). This system is used to map out the emission spectra of the nanoparticles.

2.2 Synthesis of upconverting nanoparticles

Here, we used UCNPs as nanoscale reporters of the local temperature. Specifically, we used β-$NaYF_4$ NPs co-doped with Yb^{3+} (20%) and Er^{3+} (2%) ions synthesized by a thermal decomposition method [31]. The particles have a hexagonal plate morphology with a characteristic size of 300 nm. Details on the chemical synthesis are described in the Supplementary Information.

2.3 Upconversion luminescence thermometry

The Yb^{3+}-Er^{3+} pair is a well-known couple for energy transfer upconversion luminescence [32,33] and the dual doping of the fluoride matrix with these ions makes it ideal for upconversion luminescence and in particular for the determination of the local temperature through a ratiometric spectral analysis. The closely lying $^2H_{11/2}$ and $^4S_{3/2}$ Er^{3+} energy states are thermally coupled through the Boltzmann law [11] and the integrated area of the $^2H_{11/2}\rightarrow{}^4I_{15/2}$ (I_H) and $^4S_{3/2}\rightarrow{}^4I_{15/2}$ (I_S) emission bands is used to define a ratiometric thermometric parameter $\Delta=I_H/I_S$. This parameter depends on the temperature T, the energy gap (δE) between the barycenter of the two emission bands, and a pre-exponential factor. By performing a calibration procedure in which the thermometric parameter (Δ_0) is calculated from the emission spectra at a known temperature (T_0), it is possible to calculate T at any other temperature (within the range of validity) as [9,34]:

$$\frac{1}{T} = \frac{1}{T_0} - \frac{k_B}{\delta E} ln\left(\frac{\Delta}{\Delta_0}\right) \quad (1)$$

The calibration procedure was performed by depositing the UCNPs on a controlled Peltier plate while measuring temperatures with a type K thermocouple. Calibration data are shown in Fig. 1a,c-d. In Fig. 1a, the effect of increasing the temperature on the emission spectra is the decrease of I_S while I_H remains barely constant. As a result, the thermometric parameter Δ is increased at higher temperatures. In Fig. 1c, the best linear fit of the experimental data, according to Eq. 1, results in δE=745±9 cm^{-1} where Δ_0=0.26±0.015 at T_0=297.0±0.1 K. Although the $^4H_{9/2} \rightarrow {}^4I_{13/2}$ transition is discerned in the integration range of I_S (as recently highlighted, [35,36]) this does not impact significantly on the fitted δE value that agrees with the values reported so far for β-$NaYF_4$ co-doped with Yb^{3+} (20%) and Er^{3+} (2%) ions synthesized by a thermal decomposition method [37].

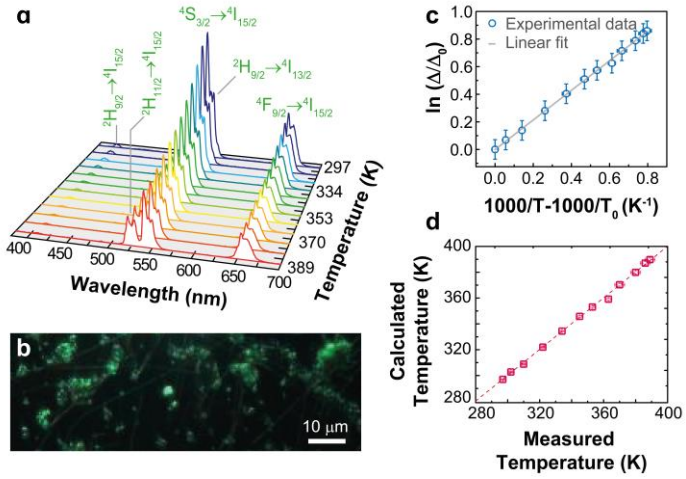

Fig. 1 (a) Emission spectra at distinct temperatures. (b) Optical image of the Yb^{3+}/Er^{3+}-UCNPs under 980 nm excitation. (c) Linearized calibration data relating the thermometric parameter Δ and the temperature T. The line is a linear fit using Eq. 1 (r^2=0.998). (d) Temperature reading using the thermocouple (measured temperature, x) versus calculated temperature (Eq. 1, y). The dashed line is a guide for the eyes corresponding to x=y.

2.4 Silver nanowires percolating network

A model nanostructure for the study of the thermal imaging method was produced by self-assembly AgNWs that were synthesized by a well-established polyol method at 130°C (details in the Supplementary Information) [38]. A water-based colloid containing AgNWs, isopropanol, and polystyrene sulphonate (PSS, molecular weight of ~70000 Da) was used to fabricate electrically percolating nanowire networks on glass slides. Two lateral electrodes were made by using silver conductive paste. By applying a continuous (DC) electric tension *V* from 0 to 9 V on these electrodes, an electrical current *I* was forced to flow producing heat dissipation due to the Joule effect. The electrical power *P*=*IV* supplied to the sample resulted in different temperature increases [23]. On top of the AgNWs network, UCNPs were deposited from a colloid containing a volatile solvent (hexane). The distribution of UCNPs and AgNWs are visualized by the electron microscopy images shown in Fig. 2a-c.

The described samples were mounted on the stage of the optical microscopy and wired for the electrothermal action through a DC tension (Fig. S1, Supporting Information). A digital amperemeter was connected to measure the current.

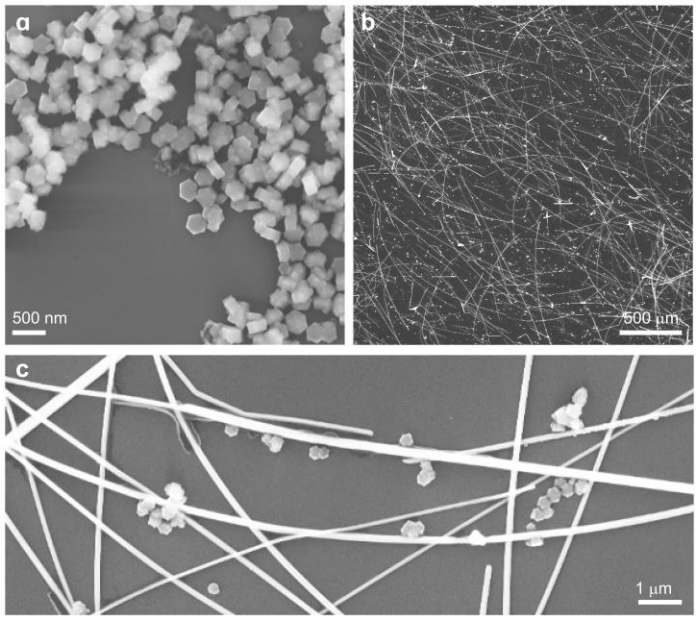

Fig. 2 Scanning electron microscopy of (a) UCNPs and (b, c) AgNWs networks containing UCNPs.

2.5 Optical and Hyperspectral Microscopy

The optical microscopy was operated under different regimes using a 50× objective lens. First, an image of the sample in dark field (DF) mode was recorded. Then, an image was taken under the sole illumination of a 980 nm laser impinging on a circular spot of approximately 200 µm diameter on the sample. The emissions from UCNPs allowed us to identify the location of individual UCNPs and clusters.

2.6 Analysis of hyperspectral images

The hyperspectral image was acquired under the same illumination conditions described above, setting the spectral bands for acquisition to cover the luminescence from 500 to 580 nm with 1.24 nm spectral resolution, accounting for 66 spectral bands in total. The constructed hyperspectral image consists of 696 × 696 pixels^2 registered line-by-line in a pitch-dark room with a total acquisition time of about 40 minutes.

After the acquisition, the hyperspectral images were postprocessed to construct maps of the emission intensity, thermometric parameter, and signal-to-noise ratio (SNR). First, a baseline correction was performed on each image by subtracting a linear baseline fitted to the off-emission wavelengths of Er^{3+} from the emission spectra. These are the data points from 500 to 515 nm and from 565 and 580 nm (Fig. S2, Supporting Information). Then, the emissions bands corresponding to the I_H and I_S transitions were calculated by integrating the emission spectra from 515 to 534 nm and from 534 to 565 nm, respectively. The total emission intensity was calculated as the sum of both bands while the thermometric parameter was calculated as the ratio between I_H and I_S. To get out of unrealistic values from low-intensity pixels, a cut-off criterion was adopted by which I_H was set to zero if its value was below a certain threshold. Hence, the thermometric parameter Δ from low emission pixels was set to zero and dismissed from the subsequent analysis.

The SNR on each pixel was calculated considering the rational described below. The experimentally detected signal intensity (s) can be physically described as the product of the detector gain (α), the quantum yield (Q) of the photon-to-electron conversion in the detector, and the number (N) of incoming photons, as described in equation 2:

$$s = \alpha Q N \qquad (2)$$

On the other hand, the dark noise (σ^{dark}) is expressed as

$$\sigma^{dark} = \alpha\beta(T)t \quad (3)$$

where β is a thermal factor dependent on the temperature of the detector and *t* is the acquisition time. Experimentally, we evaluate σ^{dark} at a given pixel, indexed as *ij,* by calculating the square differences between data points at successive wavelengths (index *k*) in the off-emission region as stated in equation 4:

$$\sigma^{dark}{}_{ij} = \frac{B^{Total}}{B^{off}} \sqrt{\sum_{k=1}^{B^{off}} \left(I_{ij}(\lambda_{k+1}) - I_{ij}(\lambda_k)\right)^2} \quad (4)$$

where B^{Total} is the total number of spectral points in the spectrum (66 bands) and B^{off} is the number of wavelengths in the off-emission region (25 bands).

In addition, considering the intensity detected as proportional to the number of collected photons, we calculate the shot noise as it is proportional to the square root of the measured intensity:

$$\sigma^{shot} = \alpha\sqrt{\overline{QN}} \propto \sqrt{\bar{I}} \quad (5)$$

Therefore, the total noise is given by:

$$\sigma^{Tot} = \sqrt{\overline{(\sigma^{dark})^2 + (\sigma^{shot})^2}} \quad (6)$$

With these components, it is possible to quantify the signal-to-noise ratio (SNR) at each pixel *ij* of the hyperspectral image as:

$$SNR_{ij} = \frac{\alpha QN}{\sqrt{(\sigma^{dark})^2 + (\sigma^{shot})^2}} \sim \frac{I_{ij}}{\sqrt{(\sigma^{dark}{}_{ij})^2 + I_{ij}}} \qquad (7)$$

3. Results and Discussion

The HSI technique was first applied on a sample containing the percolating network of AgNWs and the UCNPs on glass without application of an external electric tension between the electrodes (the sample is at room temperature). In Fig. 3 we present the results obtained after processing the data as described in the previous section. Fig. 3a shows a DF image of the explored region of the sample. The AgNWs form a percolating network with multiple junctions in close contact with the UCNPs. Individual UCNPs and clusters are located at specific regions of interest across the AgNWs network, for example, at crossing points between nanowires, along wires, or close to the extreme tips. Fig. 3b presents an intensity map constructed from the integrated spectrum at each pixel. By comparing the intensity map with the optical image of Fig. 3a it is possible to identify the location of the high-intensity points and their position relative to the AgNWs. The quality of the hyperspectral image can be analyzed through the SNR map shown in Fig. 3c. The brightest points represent those pixels with a well-defined emission spectrum where the calculation of the thermometric parameter holds a lower uncertainty. This will be used further on to calculate a weighted average of the temperature in a given cluster. Fig. 3d displays a map of the thermometric parameter, presenting a scarce variation across the map, which implies that all UCNPs are at the same temperature.

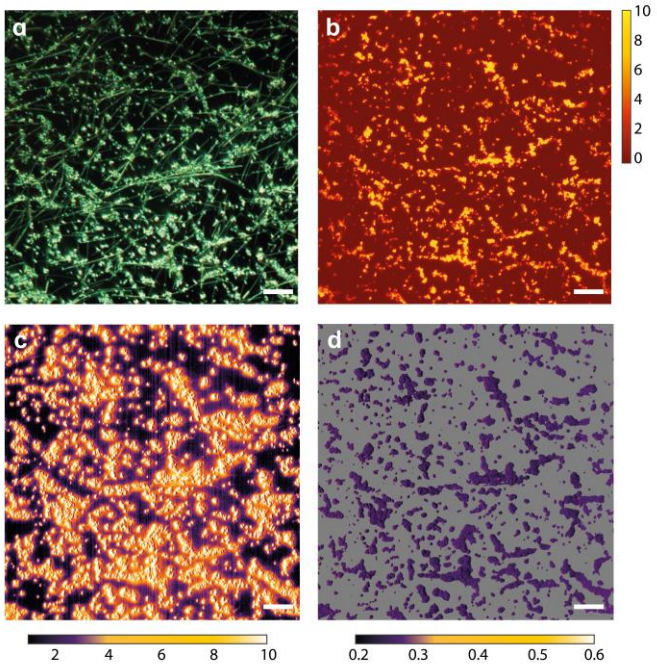

Fig. 3 (a) Optical image in dark field mode of a AgNWs network covered by UCNPs. (b-d) Maps constructed from the hyperspectral images at room temperature (applied electric tension = 0 V) and under 980 nm excitation: (b) Intensity map of UCL, (c) calculated SNR, (d) thermometric parameter Δ. Scale bars correspond to 20 μm.

We then increase the sample temperature by Joule heating imposing a DC electric tension. We repeated the procedure for the acquisition of the HSI applying 2, 4, and 6 V. The measured circulating electrical currents were 30, 70, and 110 mA, corresponding to electrical powers of 60, 280, and 660 mW, respectively. The thermal maps presented in Fig. 4b-e were produced from the HSI obtained in each case and applying the calibration curve shown in Fig. 1. As expected, higher temperatures are detected by the UCNPs at increasing applied electric tensions. The temperature profiles are fairly even across the images indicating homogeneous sample heating. However, it is worth mentioning that at least two experimental artifacts were observed: first, the right side of the thermal maps shows slightly higher temperatures; also, small variations were observed inside clusters of UCNPs. The former is highly correlated with the profiles of the emission intensity (shown in Supp. Information, Fig. S4) and it is due to misalignment of the incident laser beam and the region

scanned for the HSI acquisition. The latter is related to the SNR profiles, also shown in the Supp. Information.

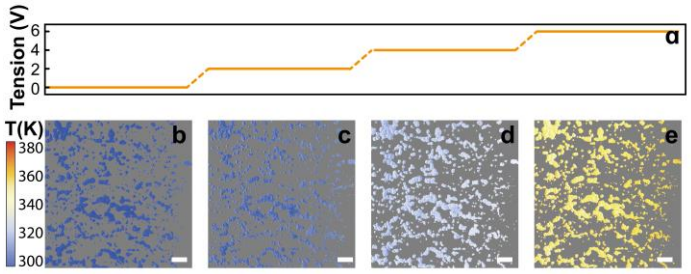

Fig. 4 a) Increasing applied electric tensions (0-6 V) and (b-e) corresponding thermal images constructed from hyperspectral images of UCNPs on AgNWs networks. The dissipated electrical powers are 0, 60, 280, and 660 mW, respectively. Scale bars correspond to 20 μm.

To analyze the temperature profiles in more detail, we performed a histogram (Fig. 5a) to evaluate the number of pixels (above the intensity threshold) at a given temperature for each electric tension. We add data from an additional sample submitted to 9 V that will be discussed in the following section (data shown in Fig. S3, Supporting Information). Temperature profiles were obtained by averaging the thermal readings across lines (Fig. 5b). A statistical analysis of quartiles allowed us to establish the mean values and confidence intervals for each case (Fig. 5c). The extracted values are displayed in Table 1.

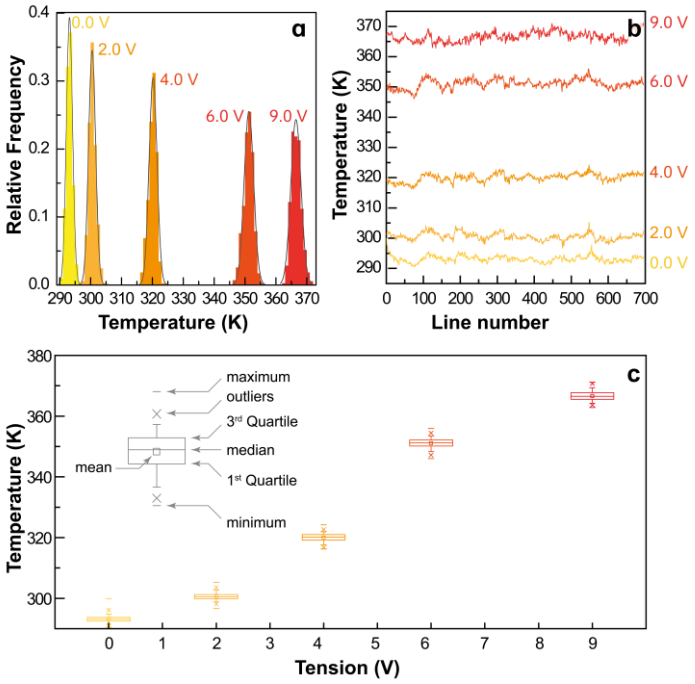

Fig. 5 (a) Histograms showing the number of pixels (normalized by the total number 696 x 696 pixels) with corresponding temperature readings. Solid lines are Gaussian distribution fits for each histogram (r^2>0.986). (b) Temperature profiles were obtained by averaging the thermal readings across lines. (c) Quartile analysis for each electric tension.

Table 1 Quartile analysis of thermal maps constructed from hyperspectral images.

Tension (±0.1V)	Current (±0.01A)	Power (W)	Q_1 (K)	Median (K)	Q3 (K)	Interquartile range (K)
0.0	0.00	0.00	292.5	293.1	293.8	1.3
2.0	0.03	0.06	299.8	300.4	301.2	1.4
4.0	0.07	0.28	319.2	320.1	321.0	1.8
6.0	0.11	0.66	350.1	351.3	352.2	2.1
9.0	0.12	1.09	365.5	366.6	367.7	2.2

Moreover, we decomposed the thermal images by averaging the temperature profiles along each column (Fig. S4). This allows a clearer view of the experimental artifacts produced by optical misalignments and statistical fluctuations. For example, the profiles across columns show a clear trend of increasing temperatures for the right side of the images. Also, the fluctuations are higher for the column profiles. This is because the hyperspectral images are constructed through a line-by-line scanning from top to bottom, meaning that averages along lines are calculated from data obtained at

the same scanning step, *i.e.* temporally close, while the column averages add as an extra factor the temporal variability of the intensities and sensitivity of the detector during the hyperspectral scanning. For this reason, we focused the statistical analyses on the line profiles at each applied electrical power as shown in Table 2. From the tabulated data one can notice, even at room temperature (293 K) with no thermal gradients expected across the sample, a very precise standard deviation of 1.06 K was attained with this method. At higher temperatures, the standard deviation increases reaching 1.57 K at 366.6 K.

Table 2 Statistical data from temperature line profiles shown in Fig. 5b.

Tension (±0.1V)	0.00	2.00	4.00	6.00	9.00
Power (W)	0.00	0.06	0.28	0.66	1.09
T_{min} (K)	290.50	296.70	316.20	346.00	362.80
T_{max} (K)	299.90	305.20	324.20	355.90	371.20
T_{mean} (K)	293.20	300.60	320.00	351.10	366.60
Mean deviation (K)	0.80	0.92	1.05	1.23	1.27
Median deviation (K)	0.62	0.71	0.86	1.01	1.08
Variance (K)	1.13	1.38	1.71	2.43	2.46
Standard Deviation (K)	1.06	1.18	1.31	1.56	1.57

3.1 Dynamic experiments for hyperspectral thermometry

To further explore the thermometric capabilities of the proposed technique, we performed dynamical experiments in which the electrical power supplied was varied during the hyperspectral image acquisition. For example, we run experiments with the sample at room temperature at the beginning of the running HSI, and subsequently applying a DC tension of 3 V was after few minutes, and again increasing 6 V after the same time Alternatively, we carried out experiments with reverse electric tension sequence. The corresponding thermal images and profiles are shown in Fig. 6 while the thermometric, SNR, and intensity maps are shown in Fig. S5 of Supporting Information.

The time progression for the thermal maps should be read from top to bottom. Therefore, we started from a readily constant temperature and observed the temperature change immediately after the modification of the applied electric tension. This demonstrates that upconversion

thermometry based on hyperspectral imaging can study thermal processes with slow dynamics, *i.e,* in the seconds to minutes range.

In the following section, we calculate the spatial and temporal resolution of the measurements. Although the constants involved in the heating processes studied here are in the timescale of a minute, faster detection can be configured, either by setting shorter integration times, reducing the scanning window size, or the number of spectral bands for acquisition.

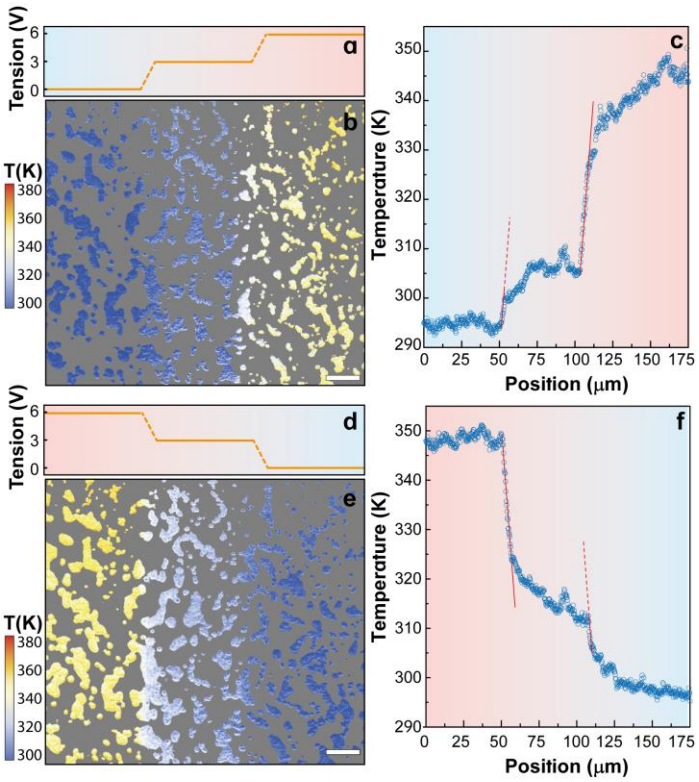

Fig. 6 Temperature maps constructed from hyperspectral images during the acquisition with applied electric tension switched from (a-b) 0 – 3 – 6 V and (d-e) 6 – 3 – 0 V. (c, f) Line averaged temperature profiles evaluated for the (b) and (e) maps respectively. The slope of all the lines (3.75±0.08 $K \cdot \mu m^{-1}$) is the same both on heating and cooling events. Scale bars correspond to 20 μm.

An additional experiment where the applied electric tension was changed from 0 to 9 V is presented in the Supporting information (Fig. S6) showing an increase in temperature from (295.9 ± 0.7) K to (364.0 ± 1.2) K.

The spatial resolution of the measurement can be calculated accordingly to the definition by [34]:

$$\delta x = \frac{\delta T}{\left|\vec{\nabla} T\right|_{max}} \qquad (8)$$

where $\left|\vec{\nabla} T\right|_{max} = \mathrm{d}T/\mathrm{d}x$ is the value of the maximum temperature gradient of the mapping and δT is its temperature uncertainty (estimated by the standard deviation of the mapping for the first 50 μm as δT=0.78 K). We notice that the maximum temperature gradient is, irrespective of the temperature being raised or decreased, always $|dT/dx|$=3.75±0.08 K·μm^{-1}, resulting in a spatial resolution of δx=0.208±0.04 μm. This is the highest spatial resolution reported so far for luminescent thermometers exceeding by a factor of ~5 the value reported for a microheater covered with a layer of UCNPs [35] and by ~2 the previous best value, obtained in a thermal mapping of an electric circuit covered with a luminescent thermometric film [39]. We can also calculate the temporal resolution of the measurement knowing that the 696 lines take 40 minutes to acquire, which corresponds to a mean scan time per line of 3.4 s. Converting the line number in time, we can reconstruct the temporal profile displaying a maximum slope of dT/dt = 0.180±0.006 K·s^{-1}. Using the definition of temporal resolution [34]:

$$\delta t = \frac{\delta T}{|dT/dt|_{max}} \qquad (9)$$

we calculate the temporal resolution of the measurement as δt=4.3±0.1 s. Although this value is 1000 times higher than the best one reported so far (4.8 ms), we note, however, that we are not reaching the time limit of the hyperspectral setup. The experiments described in this work were designed to improve only the spatial resolution. We can improve δt at the cost of the decrease of the spatial resolution by fixing the hyperspectral system in a central position of the image and record the time-dependent emission spectra that will be converted into temperature using the abovementioned procedure. The expected ultimate time resolution of this measurement is dependent on the

integration time of the hyperspectral system, which can be tuned for these UCNPs particles to values down to 100 ms.

Spatially resolved thermal imaging

The spatial correlation between the thermal readings and the locations within the AgNWs where heat was generated can be extracted from the direct comparison between the DF optical images and the thermal maps constructed from HSI. This was done for a sample submitted to an applied external DC electric tension of 9 V. Here, the thermal readings of selected clusters of UCNPs, comprising multiple neighboring pixels, was evaluated considering the SNR of each pixel and performing a weighted average as

$$\tilde{\Delta}_{cluster} = \frac{\sum_{p=1}^{N} \Delta_p SNR_p}{\sum_{p=1}^{N} SNR_p} \qquad (10)$$

where $\tilde{\Delta}_{cluster}$ is the average value of the corresponding cluster formed by *N* countable pixels using the index *p.* Using this method, the thermal readings from well-defined pixels, *i.e.* with high SNR, are the dominant components in the weighted sum. The corresponding weighted average temperature, $\widetilde{\mathrm{T}}_{\mathrm{cluster}}$, was calculated using Eq. 1. With this approach, we attempted to identify hot spots or thermal gradients that could be related to specific regions within the AgNWs network. Fig. 7 shows a few examples of this approach. In particular, we closely explore regions of crossing NWs (points numbered 4, 5, 7 and 11), where the junctions could dissipate more heat due to higher contact resistance,[30] or, on the contrary, isolated UCNPs or clusters, not in contact with AgNWs (3, 6 and 10) that were expected to show lower temperatures. Other regions of interest were spotted, for example, at the ends of an NW (8) or slightly away from a crossing point (9). Furthermore, we spotted several clusters along the same NW (indexed in yellow in Fig. 7) to inquire if a single NW displays an isothermal status or not. Points 2 and 4 can be considered as well as being in contact with this particular NW.

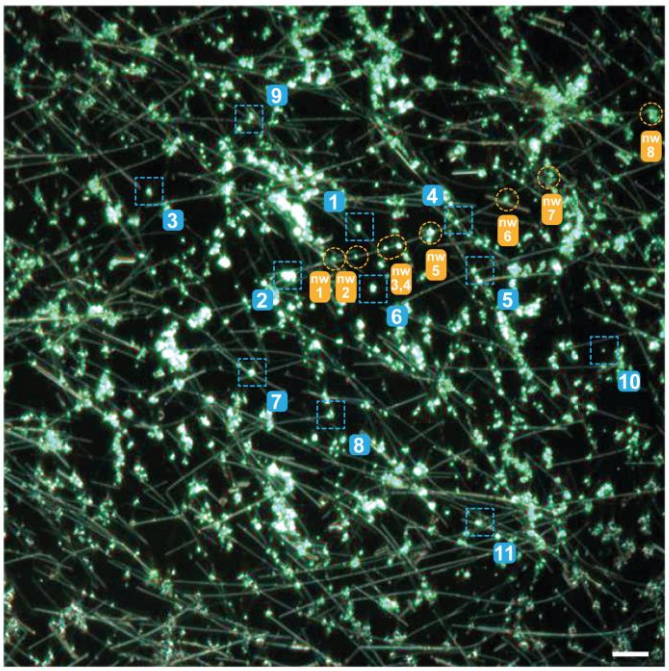

Fig. 7 Darkfield optical image of an AgNWs network covered with UCNPs under an applied electric tension of 9 V (1.09 W) and excited at 980 nm. Selected points of interest are highlighted by the blue squares and numbered. Clusters along the same NW are highlighted by yellow circles. The scale bar corresponds to 10 μm.

The spectroscopic information obtained from the HSI for each cluster is shown in Fig. S7, where the cropped intensity, thermometric parameter, and SNR maps, were used to calculate the weighted average values tabulated in Table 3. The temperature map and the information corresponding to the clusters along the individual NW are shown in Fig. S8 and S9, Supporting information, respectively.

The extracted information and the results of the analysis performed, however, do not show with clarity the presence of thermal gradients or the identification of hot spots. Indeed, comparing the acquisition time per line (3.4 s) with the characteristic thermalization time of nanowires with the dimensions of those studied here (<1 ns), we conclude that, at the time scale of hyperspectral image measurement per line, the nanowires are totally thermalized and so the percolating network is isothermal from the hyperspectral image point of view. The calculated temperatures show random variations within ±3 K of a mean temperature of 369 K. Outlier values of 359.6 K (#10) and 376.2 K (#8) were also observed and can be explained by their lower emission intensity. By random

variations, we mean that the calculated temperatures are not obviously correlated with the locations within the AgNWs network. For example, clusters at crossing points display temperatures below and above the mean value, ruling out a clear trend pointing to hot spots. On the other hand, the isolated clusters show temperatures that are, in most cases, below the mean value with some fluctuations between them.

Table 3 Weighted averaged thermometric parameter ($\widetilde{\boldsymbol{\Delta}}_{\mathbf{cluster}}$) and temperature ($\widetilde{\mathbf{T}}_{\mathbf{cluster}}$) of the corresponding clusters highlighted in Fig. 7.

# Cluster	1	2	3	4	5	6	7	8	9	10	11
$\widetilde{\Delta}_{cluster}$	0.540	0.507	0.525	0.515	0.546	0.523	0.527	0.559	0.527	0.49	0.544
$\widetilde{T}_{cluster}$ (K)	371.5	363.7	368.1	365.7	373.0	367.5	368.4	376.2	368.5	359.6	372.7
# Cluster	nw1	nw2	nw3	nw4	nw5	nw6	nw7	nw8	—	—	—
$\widetilde{\Delta}_{cluster}$	0.538	0.550	0.508	0.513	0.522	0.528	0.540	0.533	—	—	—
$\widetilde{T}_{cluster}$ (K)	371.1	374.0	363.9	365.1	367.4	368.8	371.7	370.0	—	—	—

Regarding the clusters along the individual NW, temperature readings indicate important fluctuations between selected spots but are not obviously related to their specific location. Crossing points (nw1 and nw7) show higher temperatures, but cluster 4, also in a crossing point with this NW, shows a temperature 4 K lower. Clusters at opposite ends of the NW (2 and nw8) show a temperature difference of more than 6 K.

Overall, the thermal readings across the hyperspectral image can be ascribed to statistical fluctuations, limiting the sensitivity of the technique to spatially resolved local temperature gradients or heating effects. Further studies using UCNPs of smaller size are in progress to produce a homogeneous covering and, therefore, improve the spatial and thermal resolution of the proposed technique.

4. Conclusion

A thermographic technique that combines upconversion luminescence with hyperspectral imaging was developed. The method was applied to study the electrothermal effect of AgNWs percolating networks using large-size (~300 nm) Er^{3+}/Yb^{3+}-doped UCNPs as luminescent thermometers. A post-processing algorithm was developed to analyze the hyperspectral information and construct thermal and signal-to-noise ratio maps. The thermal readings across the hyperspectral image show statistical

fluctuations that limit the thermal sensitivity of the technique. Besides, the formation of large and disperse clusters of the UCNPs undermine the spatial resolution, which precludes its use for the observation of local temperature gradients or heating effects. However, the thermal images were successful in quantifying the electrothermal action of AgNWs networks when external electric tensions are applied. Furthermore, thermal evolution when the electrothermal heating was turned on or off was clearly observed, enabling its use for the study of slow-dynamical thermal processes. The spatial resolution of the measurements, 0.208±0.004 μm, is the best value reported so far using luminescent thermometry. Optimization of the thermometric UCNPs and the experimental set-up for acquiring faster hyperspectral images are sought to improve the accuracy and resolution of the proposed method.

Acknowledgments

This work was supported and performed under the auspices of FAPESP through Grants #2011/19924-2, #2012/04870-7, #2012/05903-6, #2015/21290-2, #2015/21289-4, and #2017/10581-1. EDM was the beneficiary of a post-doctoral FAPESP fellowship #2015/23882-4 during part of the development of this work. RRU acknowledges CNPq Grant No 309483/2018-2. EDM acknowledges funding from ANPCyT-FONCyT PICT 2017-0307. Research supported by LNNano-Brazilian Nanotechnology National Laboratory (CNPEM/MCTI) during the use of the electron microscopy open-access facility. This work was also developed within the scope of the project CICECO – Aveiro Institute of Materials, UIDB/50011/2020, financed by Portuguese funds through the FCT/MEC and when appropriate co-financed by FEDER under the PT2020 Partnership Agreement. Financial support from the European Union (Horizon 2020 FET Open program, grant agreement no. 801305) and Portuguese Science Foundation, FCT (NANOHEATCONTROL - POCI-01-0145-FEDER-031469) are acknowledged. This work was initiated at IFGW-UNICAMP, Brazil, and finished at the current affiliation of the corresponding author.

References

[1] R. Qian, X. Gong, H. Xue, W. Lu, L. Zhu, Z. An, Developments on Thermometric Techniques in Probing Micro- and Nano-heat, ES Energy Environ. (2019) 4–17. https://doi.org/10.30919/esee8c369.

[2] M.M. Kim, A. Giry, M. Mastiani, G.O. Rodrigues, A. Reis, P. Mandin, Microscale thermometry: A review, Microelectron. Eng. 148 (2015) 129–142. https://doi.org/10.1016/j.mee.2015.11.002.

[3] P.R.N. Childs, Chapter 1: Nanoscale thermometry and temperature measurement, RSC Nanosci. Nanotechnol. (2016) 3–22. https://doi.org/10.1039/9781782622031-00001.

[4] K. Kim, W. Jeong, W. Lee, P. Reddy, Ultra-High Vacuum Scanning Thermal Microscopy for Nanometer Resolution Quantitative Thermometry, ACS Nano. 6 (2012) 4248–4257. https://doi.org/10.1021/nn300774n.

[5] F. Menges, P. Mensch, H. Schmid, H. Riel, A. Stemmer, B. Gotsmann, Temperature mapping of operating nanoscale devices by scanning probe thermometry, Nat. Commun. 7 (2016) 10874. https://doi.org/10.1038/ncomms10874.

[6] Q. Weng, S. Komiyama, L. Yang, Z. An, P. Chen, S.A. Biehs, Y. Kajihara, W. Lu, Imaging of nonlocal hot-electron energy dissipation via shot noise, Science 360 (2018) 775–778. https://doi.org/10.1126/science.aam9991.

[7] H. Suo, X. Zhao, Z. Zhang, Y. Wang, J. Sun, M. Jin, C. Guo, Rational Design of Ratiometric Luminescence Thermometry Based on Thermally Coupled Levels for Bioapplications, Laser Photon. Rev. 15 (2021) 2000319. https://doi.org/10.1002/lpor.202000319.

[8] J.D. Kilbane, E.M. Chan, C. Monachon, N.J. Borys, E.S. Levy, A.D. Pickel, J.J. Urban, P.J. Schuck, C. Dames, Far-field optical nanothermometry using individual sub-50 nm upconverting nanoparticles, Nanoscale. 8 (2016) 11611–11616. https://doi.org/10.1039/c6nr01479h.

[9] C.D.S. Brites, S. Balabhadra, L.D. Carlos, Lanthanide-Based Thermometers: At the Cutting-Edge of Luminescence Thermometry, Adv. Opt. Mater. 7 (2019) 1801239. https://doi.org/10.1002/adom.201801239.

[10] O.A. Savchuk, J.J. Carvajal, C.D.S. Brites, L.D. Carlos, M. Aguilo, F. Diaz, Upconversion thermometry: A new tool to measure the thermal resistance of nanoparticles, Nanoscale. 10 (2018) 6602–6610. https://doi.org/10.1039/c7nr08758f.

[11] M. Suta, A. Meijerink, A Theoretical Framework for Ratiometric Single Ion Luminescent Thermometers - Thermodynamic and Kinetic Guidelines for Optimized Performance, Adv. Theory Simulations. 3 (2020) 1–32. https://doi.org/10.1002/adts.202000176.

[12] L. Gao, R.T. Smith, Optical hyperspectral imaging in microscopy and spectroscopy – A review of data acquisition, J. Biophotonics. 8 (2015) 441–456. https://doi.org/10.1002/jbio.201400051.

[13] G.A. Roth, S. Tahiliani, N.M. Neu-Baker, S.A. Brenner, Hyperspectral microscopy as an analytical tool for nanomaterials, Wiley Interdiscip. Rev. Nanomedicine Nanobiotechnology. 7 (2015) 565–579. https://doi.org/10.1002/wnan.1330.

[14] N. Panov, D. Lu, E. Ortiz-Rivero, E. Martinazzo Rodrigues, P. Haro-González, D. Jaque, E. Hemmer, Hyperspectral Imaging and Optical Trapping: Complementary Tools for Assessing Direction-Dependent Polarized Emission from Single Upconverting $LiYF_4$:Yb^{3+}/Er^{3+} Microparticles, Adv. Opt. Mater. 9 (2021) 2100101. https://doi.org/10.1002/adom.202100101.

[15] E.M. Rodrigues, N. Rutajoga, D. Rioux, J. Yvon-Leroux, E. Hemmer, Hyperspectral Imaging as a Tool to Study Optical Anisotropy in Lanthanide-Based Molecular Single Crystals, J. Vis. Exp. (2020). https://doi.org/10.3791/60826.

[16] R. Marin, I. Halimi, D. Errulat, Y. Mazouzi, G. Lucchini, A. Speghini, M. Murugesu, E. Hemmer, Harnessing the Synergy between Upconverting Nanoparticles and Lanthanide Complexes in a Multiwavelength-Responsive Hybrid System, ACS Photonics. 6 (2019) 436–445. https://doi.org/10.1021/acsphotonics.8b01381.

[17] D. Errulat, B. Gabidullin, M. Murugesu, E. Hemmer, Probing Optical Anisotropy and Polymorph-Dependent Photoluminescence in [Ln_2] Complexes by Hyperspectral Imaging on Single Crystals, Chem. - A Eur. J. 24 (2018) 10146–10155. https://doi.org/10.1002/chem.201801224.

[18] Y. Huang, Y. Tian, C. Hang, Y. Liu, S. Wang, M. Qi, H. Zhang, Q. Peng, TiO_2-Coated Core-Shell Ag Nanowire Networks for Robust and Washable Flexible Transparent Electrodes, ACS Appl. Nano Mater. 2 (2019) 2456–2466. https://doi.org/10.1021/acsanm.9b00337.

[19] Q. Xue, W. Yao, J. Liu, Q. Tian, L. Liu, M. Li, Q. Lu, R. Peng, W. Wu, Facile Synthesis of Silver Nanowires with Different Aspect Ratios and Used as High-Performance Flexible Transparent Electrodes, Nanoscale Res. Lett. 12 (2017) 480. https://doi.org/10.1186/s11671-017-2259-6.

[20] Y. Jin, Y. Sun, K. Wang, Y. Chen, Z. Liang, Y. Xu, F. Xiao, Long-term stable silver nanowire transparent composite as bottom electrode for perovskite solar cells, Nano Res. 11 (2018) 1998–2011. https://doi.org/10.1007/s12274-017-1816-8.

[21] S.R. Kim, J.H. Kim, J.W. Park, Wearable and Transparent Capacitive Strain Sensor with High Sensitivity Based on Patterned Ag Nanowire Networks, ACS Appl. Mater. Interfaces. 9 (2017) 26407–26416. https://doi.org/10.1021/acsami.7b06474.

[22] E.D. Martínez, J.H. Lohr, M. Sirena, R.D. Sánchez, H. Pastoriza, Silver nanowires in poly(methyl methacrylate) as a conductive nanocomposite for microfabrication, Flex. Print. Electron. 1 (2016) 1–10. https://doi.org/10.1088/2058-8585/1/3/035003.

[23] E.D. Martínez, A.F. García Flores, H. Pastoriza, R.R. Urbano, C. Rettori, Electrothermal silver nanowire thin films for In-Situ observation of thermally-driven chemical processes, Sensors Actuators B Chem. 259 (2018) 475–483. https://doi.org/10.1016/j.snb.2017.12.021.

[24] C. Celle, C. Mayousse, E. Moreau, H. Basti, A. Carella, J.P. Simonato, Highly flexible transparent film heaters based on random networks of silver nanowires, Nano Res. 5 (2012) 427–433. https://doi.org/10.1007/s12274-012-0225-2.

[25] J. Li, J. Liang, X. Jian, W. Hu, J. Li, Q. Pei, A flexible and transparent thin film heater based on a silver nanowire/heat-resistant polymer composite, Macromol. Mater. Eng. 299 (2014) 1403–1409. https://doi.org/10.1002/mame.201400097.

[26] T. Kim, Y.W. Kim, H.S. Lee, H. Kim, W.S. Yang, K.S. Suh, Uniformly interconnected silver-nanowire networks for transparent film heaters, Adv. Funct. Mater. 23 (2013) 1250–1255. https://doi.org/10.1002/adfm.201202013.

[27] E.D. Martínez, C.D.S. Brites, L.D. Carlos, A.F. García-Flores, R.R.R. Urbano, C. Rettori, Electrochromic Switch Devices Mixing Small- and Large-Sized Upconverting Nanocrystals, Adv. Funct. Mater. 29 (2019) 1807758. https://doi.org/10.1002/adfm.201807758.

[28] H.H. Khaligh, L. Xu, A. Khosropour, A. Madeira, M. Romano, C. Pradére, M. Tréguer-Delapierre, L. Servant, M.A. Pope, I.A. Goldthorpe, The Joule heating problem in silver nanowire transparent electrodes, Nanotechnology. 28 (2017). https://doi.org/10.1088/1361-6528/aa7f34.

[29] T. Bin Song, Y. Chen, C.H. Chung, Y. Yang, B. Bob, H.S. Duan, G. Li, K.N. Tu, Y. Huang, Nanoscale joule heating and electromigration enhanced ripening of silver nanowire contacts, ACS Nano. 8 (2014) 2804–2811. https://doi.org/10.1021/nn4065567.

[30] A.T. Bellew, H.G. Manning, C. Gomes da Rocha, M.S. Ferreira, J.J. Boland, Resistance of Single Ag Nanowire Junctions and Their Role in the Conductivity of Nanowire Networks, ACS Nano. 9 (2015) 11422–11429. https://doi.org/10.1021/acsnano.5b05469.

[31] X. Ye, J.E. Collins, Y. Kang, J. Chen, D.T.N. Chen, A.G. Yodh, C.B. Murray, Morphologically controlled synthesis of colloidal upconversion nanophosphors and their shape-directed self-assembly, Proc. Natl. Acad. Sci. U. S. A. 107 (2010) 22430–22435. https://doi.org/10.1073/pnas.1008958107.

[32] A. Nadort, J. Zhao, E.M. Goldys, Lanthanide upconversion luminescence at the nanoscale: Fundamentals and optical properties, Nanoscale. 8 (2016) 13099–13130. https://doi.org/10.1039/c5nr08477f.

[33] J. Zhou, Q. Liu, W. Feng, Y. Sun, F. Li, Upconversion luminescent materials: Advances and applications, Chem. Rev. 115 (2015) 395–465. https://doi.org/10.1021/cr400478f.

[34] C.D.S. Brites, A. Millán, L.D. Carlos, Lanthanides in Luminescent Thermometry, Handb. Phys. Chem. Rare Earths. 49 (2016) 339–427. https://doi.org/10.1016/bs.hpcre.2016.03.005.

[35] T.P. Van Swieten, T. Van Omme, D.J. Van Den Heuvel, S.J.W. Vonk, R.G. Spruit, F. Meirer, H.H.P. Garza, B.M. Weckhuysen, A. Meijerink, F.T. Rabouw, R.G. Geitenbeek, Mapping Elevated Temperatures with a Micrometer Resolution Using the Luminescence of Chemically

Stable Upconversion Nanoparticles, ACS Appl. Nano Mater. 4 (2021) 4208–4215. https://doi.org/10.1021/acsanm.1c00657.

[36] J.C. Martins, A.R.N. Bastos, R.A.S. Ferreira, X. Wang, G. Chen, L.D. Carlos, Primary Luminescent Nanothermometers for Temperature Measurements Reliability Assessment, Adv. Photonics Res. 2 (2021) 2000169. https://doi.org/10.1002/adpr.202000169.

[37] F. Wang, R. Deng, X. Liu, Preparation of core-shell NaGdF4 nanoparticles doped with luminescent lanthanide ions to be used as upconversion-based probes, Nat. Protoc. 9 (2014) 1634–1644. https://doi.org/10.1038/nprot.2014.111.

[38] J. Jiu, T. Araki, J. Wang, M. Nogi, T. Sugahara, S. Nagao, H. Koga, K. Suganuma, E. Nakazawa, M. Hara, H. Uchida, K. Shinozaki, Facile synthesis of very-long silver nanowires for transparent electrodes, J. Mater. Chem. A. 2 (2014) 6326–6330. https://doi.org/10.1039/C4TA00502C.

[39] C.D.S. Brites, P.P. Lima, N.J.O. Silva, A. Millán, V.S. Amaral, F. Palacio, L.D. Carlos, Organic-Inorganic Eu^{3+}/Tb^{3+} codoped hybrid films for temperature mapping in integrated circuits, Front. Chem. 1 (2013) 1–6. https://doi.org/10.3389/fchem.2013.00009.